












Article

Influence of Contacts and Applied Voltage on a Structure of a Single GaN Nanowire

Sergey Lazarev ^{1,2,*} , Young Yong Kim ^{1,†} , Luca Gelisio ^{1,‡} , Zhaoxia Bi ³ , Ali Nowzari ³,
Ivan A. Zaluzhnyy ^{1,‡} , Ruslan Khubbutdinov ^{1,4}, Dmitry Dzhigaev ^{1,§} , Arno Jeromin ⁵, Thomas F. Keller ^{5,6} ,
Michael Sprung ¹ , Anders Mikkelsen ³ , Lars Samuelson ³  and Ivan A. Vartanyants ^{1,4,*} 

- ¹ Deutsches Elektronen-Synchrotron DESY, Notkestraße 85, 22607 Hamburg, Germany; young.yong.kim@xfel.eu (Y.Y.K.); luca.gelisio@xfel.eu (L.G.); ivan.zaluzhnyy@uni-tuebingen.de (I.A.Z.); ruslan.khubbutdinov@desy.de (R.K.); dmitry.dzhigaev@sljus.lu.se (D.D.); michael.sprung@desy.de (M.S.)
- ² National Research Tomsk Polytechnic University (TPU), Lenin Avenue 30, 634050 Tomsk, Russia
- ³ Department of Physics and NanoLund, Lund University, P.O. Box 118, SE-221 00 Lund, Sweden; zhaoxia.bi@ftf.lth.se (Z.B.); anowzary@gmail.com (A.N.); anders.mikkelsen@sljus.lu.se (A.M.); lars.samuelson@ftf.lth.se (L.S.)
- ⁴ National Research Nuclear University MEPhI (Moscow Engineering Physics Institute), Kashirskoe Shosse 31, 115409 Moscow, Russia
- ⁵ Centre for X-ray and Nano Science (CXNS), Deutsches Elektronen-Synchrotron DESY, Notkestraße 85, 22607 Hamburg, Germany; arno.jeromin@desy.de (A.J.); thomas.keller@desy.de (T.F.K.)
- ⁶ Physics Department, University of Hamburg, 20355 Hamburg, Germany
- * Correspondence: dr.s.lazarev@gmail.com (S.L.); ivan.vartanyants@desy.de (I.A.V.)
- † Current Address: European XFEL GmbH, Holzkoppel 4, 22869 Schenefeld, Germany.
- ‡ Current Address: Institut für Angewandte Physik, Universität Tübingen, Auf der Morgenstelle 10, 72076 Tübingen, Germany.
- § Current Address: Division of Synchrotron Radiation Research and NanoLund, Department of Physics, Lund University, P.O. Box 118, SE-221 00 Lund, Sweden.



Citation: Lazarev, S.; Kim, Y.Y.; Gelisio, L.; Bi, Z.; Nowzari, A.; Zaluzhnyy, I.A.; Khubbutdinov, R.; Dzhigaev, D.; Jeromin, A.; Keller, T.F.; et al. Influence of Contacts and Applied Voltage on a Structure of a Single GaN Nanowire. *Appl. Sci.* **2021**, *11*, 9419. <https://doi.org/10.3390/app11209419>

Academic Editors: Atsushi Mase, Söndes Bauer and Vaclav Holý

Received: 20 August 2021
Accepted: 26 September 2021
Published: 11 October 2021

Publisher's Note: MDPI stays neutral with regard to jurisdictional claims in published maps and institutional affiliations.



Copyright: © 2021 by the authors. Licensee MDPI, Basel, Switzerland. This article is an open access article distributed under the terms and conditions of the Creative Commons Attribution (CC BY) license (<https://creativecommons.org/licenses/by/4.0/>).

Abstract: Semiconductor nanowires (NWs) have a broad range of applications for nano- and optoelectronics. The strain field of gallium nitride (GaN) NWs could be significantly changed when contacts are applied to them to form a final device, especially considering the piezoelectric properties of GaN. Investigation of influence of the metallic contacts on the structure of the NWs is of high importance for their applications in real devices. We have studied a series of different type of contacts and influence of the applied voltage bias on the contacted GaN NWs with the length of about 3 to 4 micrometers and with two different diameters of 200 nm and 350 nm. It was demonstrated that the NWs with the diameter of 200 nm are bend already by the interaction with the substrate. For all GaN NWs, significant structural changes were revealed after the contacts deposition. The results of our research may contribute to the future optoelectronic applications of the GaN nanowires.

Keywords: GaN nanowires; Bragg coherent diffraction; piezoelectric effect; finite element method

1. Introduction

Low-dimensional semiconductor material structures, such as nanowires (NWs), have developed into one of the most intensely studied fields of science and technology. One reason for the very intense research in this field is motivated by what can be offered to main-stream semiconductor technology, by which ultrahigh performing electronics (for example, transistors) and photonics (for example, photovoltaics, photodetectors, or LEDs) technologies can be merged with silicon and complementary metal–oxide–semiconductor (CMOS) technology. Semiconductor gallium nitride (GaN) NWs are promising candidates for a number of applications, such as light emitting diodes (LED), transistors, single photon sources, low-cost solar cells, etc. (see for review [1–9]). Contacting process of the nanostructures in a final optoelectronic device may lead to significant strain that changes the band gap of the final device and hence its properties. In addition, small dimensions

and high surface to volume ratio of the NWs result in higher piezoelectric effects, which influence the electron-hole recombination.

The nanostructures are commonly analyzed by the laboratory table-top equipment employing different techniques such as scanning electron microscopy (SEM), atomic force microscopy (AFM), transmission electron microscopy (TEM), laboratory X-ray diffraction (XRD), etc. In most of the cases, these methods have limitations, which do not allow investigation of the local structure of a single object along the whole NW with high resolution. Modern 3rd generation synchrotron facilities allow investigation of individual nanostructures with intense, highly-coherent, focused down to sub-micrometer scale X-ray beams. Various coherent X-ray diffraction techniques, such as coherent diffraction imaging (CDI), Bragg CDI, and ptychography may provide an important information about the three-dimensional (3D) strain field and deformation of a single nanostructure with a high spatial resolution [10–14].

The Bragg CDI is a lensless imaging technique that makes use of the coherence properties of the X-ray beam. When a finite object is illuminated by a coherent X-ray beam in Bragg geometry, interference between the incoming wavefront and the scattered beams generate a diffraction pattern, which can be recorded in the far-field by a 2D detector with proper sampling [15]. By rotating the sample in the vicinity of the Bragg angle and recording 2D diffraction patterns, one can measure a full 3D diffraction pattern and then use iterative algorithms [16,17] to determine the 3D shape and strain field in a sample. A complex amplitude object is reconstructed, whose modulus is directly related to the sample's crystalline shape and its phase is given by the projection of the displacement field on the scattering vector [18]. This allows to determine unique information about the strain field in nanosamples under different external conditions [19–21].

In our previous study [22], we analyzed the NWs of the 350–400 nm diameter with one type of contacts. We have demonstrated that deposition of the Au contacts, as well as the applied voltage bias deform single GaN nanowires leading to their bending. It was also demonstrated that the arching of the nanostructures may reach the critical value, when the NW is broken. In our current study, we analyzed NWs of the two different diameters of 200 nm and 350 nm, as well as we investigated the influence of the various type of contacts and applied voltage on the strain field and structure of these NWs.

2. Experiment

2.1. Samples

The samples with GaN NWs were prepared at the NanoLund Laboratory at Lund University, Sweden. The GaN NWs with the lengths from 3 μm to 4 μm and two different diameters of 200 nm and 350 nm were grown by selective area metal-organic vapor phase epitaxy (MOVPE), equipped with a 3×2 close-coupled showerhead reactor [23]. First, a 1 μm thick [0001]-oriented GaN template layer was grown on top of a Si (111) substrate, on which a 30 nm thick SiN_x film was deposited as a growth mask by low-pressure chemical vapor deposition (CVD). Further, hexagonal arrays of openings were defined in the SiN_x mask by e-beam lithography and reactive ion etching with the opening diameter of about 100 nm and the pitch of 1 μm . The as-patterned templates were then loaded into the MOVPE reactor to grow the GaN nanowires. Due to the growth selectivity, the GaN growth only took place from the GaN surface exposed in the SiN_x openings. The continuously supplied flows of NH_3 and triethylgallium were used to synthesize GaN nanowires. A low V/III ratio had to be used in order to achieve the nanowire geometry with vertical m-plane side facets. The triethylgallium flow was 19 $\mu\text{mol}/\text{min}$ and the growth temperature was 1042 $^\circ\text{C}$. The as-grown GaN nanowires, having a hexagonal cross-section, were about 200 nm thick and about 3.5 μm long. In order to further increase the diameter of GaN nanowires, a GaN shell was grown around the GaN nanowires. This was achieved by increasing the V/III ratio, which enhanced the GaN growth on the m-plane side facets through forming low-growth-rate facets 10 $\bar{1}$ 1 at the nanowire tip. By controlling the shell growth time, GaN nanowires with a diameter of 350 nm were obtained. From our previous

study [22], we know that the structure of GaN NWs is pure wurtzite almost without dislocations and stacking faults.

After the growth, GaN NWs were removed from the original substrate and deposited on a Si (111) chip with a 100 nm thermally grown SiO_2 layer on top, as an insulating layer. The SEM images of the free-lying NWs are presented in Figure 1. The SEM images of the NWs presented in this work were obtained in NanoLund and DESY NanoLab [24].

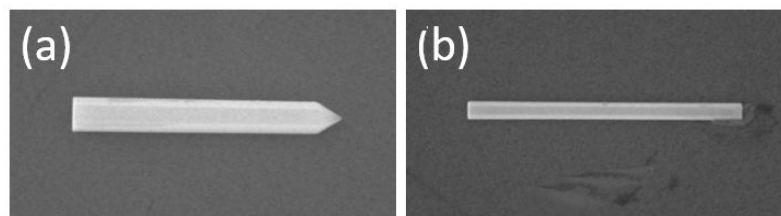


Figure 1. SEM images of the free-lying GaN NWs with the diameters of 350 nm (a) and 200 nm (b).

2.2. Contacts

After the growth and deposition, Au contacts of two different types were used to connect the GaN NWs in order to study the influence of the applied voltage on their structure. The first contacting approach was similar to our previous work [22]. The position and orientation of the NWs were random with respect to the main contacts on the substrate after their deposition. We developed a sample holder, which provided the electrical connection to the selected single NWs. The free-lying GaN NWs were connected from two sides to the power supply via pads and solid wires using different contacting methods (see Supplementary Materials). The 220 nm thick metallic contacts were deposited by electron beam lithography and thermal evaporation of Ti and Au. First, a 20 nm thick layer of Ti was deposited on SiO_2 and GaN NW to provide good adhesion between Au and GaN, and then 200 nm thick layer of Au on top of Ti layer. The SEM images of the 350 nm and 200 nm NWs contacted using this method are shown in Figure 2a,b. In comparison to our previous experiment [22], these Au contacts had larger width and were thicker. The contacts were covering a larger part of the NWs at the bottom, while the tip of the NWs was covered less. These variations in contacting geometry define the possible difference in properties of the electronic system “GaN NW + Au contacts”.

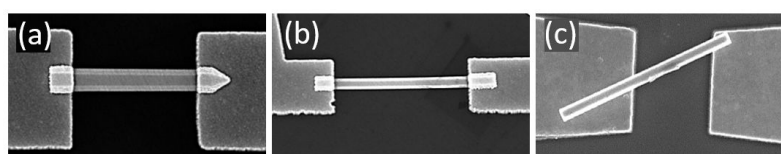


Figure 2. SEM images of the GaN NWs with the diameters of 350 nm (a) and 200 nm (b) contacted by the Au electrodes deposited above the NWs. (c) The NW with the diameter of 200 nm contacted on the top of the Au electrodes by melting procedure (see text for details).

The second type of contacts was manufactured differently. The Au contacts were deposited on the SiO_2 layer using the similar lithography technique from two sides leaving a gap between them. Further, GaN NWs were positioned on the top of these contacts and were slightly melted into the contacts by the increased temperature of 400 °C for 20 min. The SEM image of this type of contacts is shown in Figure 2c.

We performed electrical measurements before the experiment. The resistance of the system “GaN NW + Au contacts” was about 10^{12} Ohm. Therefore, the current through the NWs was relatively low, and additional cooling of the sample was not necessary.

2.3. Experimental Setup

The nanostructures were investigated at the coherence applications beamline P10 at the PETRA III synchrotron facility (DESY, Hamburg, Germany). The geometry of the

experiment is shown in Figure 3. The measurements were performed at the six-circle diffractometer equipped with a two-dimensional (2D) X-ray pixel detector EIGER X 4M positioned 1.74 m downstream from the sample in Bragg geometry. The detector had 2070×2167 pixels with the pixel size of $75 \times 75 \mu\text{m}^2$. To reduce air scattering, an evacuated flight tube was mounted between the sample and detector.

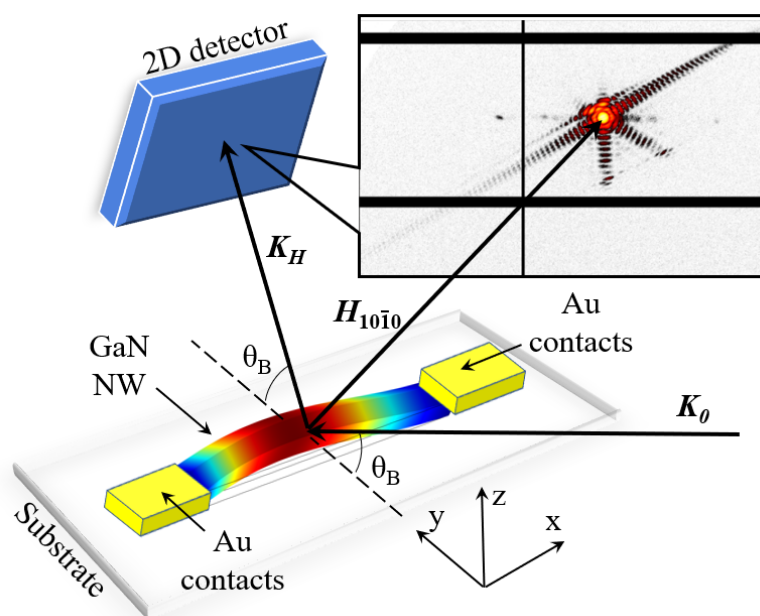


Figure 3. The experimental setup showing the incoming and diffracted beams with the wave vectors K_0 and K_H and a reciprocal lattice vector $H_{10\bar{1}0}$ of the NW that is perpendicular to the Si substrate. The sample is rotated around the Bragg angle θ_B of $10\bar{1}0$ GaN reflection. The rectangular coordinate system has z-axis perpendicular to the substrate, x-axis along, and y-axis perpendicular to the NW. In the inset, the intensity distribution of a typical free-lying NW recorded by a 2D detector is shown.

The X-ray beam with the photon energy of 9.04 keV and flux of about 10^{11} ph/s was focused at the sample using compound refractive lenses (CRLs). Characterization of the focus was performed by the knife edge scan at the sample position. The X-ray beam was about $3 \times 2 \mu\text{m}^2$ ($V \times H$) in size at full width at half maximum (FWHM). The sample with GaN NWs was mounted on the diffractometer by a specially manufactured adapter with wires connected to a voltage power supply (see for details Ref. [22]). During the experiment, $10\bar{1}0$ Bragg reflection of GaN was measured employing the incoming and diffracted X-ray beams with the wave vectors K_0 and K_H and a reciprocal lattice vector $H_{10\bar{1}0}$ of the GaN NW being normal to the substrate (see Figure 3). The sample was positioned at a Bragg angle θ_B of $10\bar{1}0$ GaN reflection and the detector was placed at $2\theta_B$ with respect to the incident X-ray beam. The rectangular coordinate system was chosen to have the z-axis perpendicular to the substrate, x-axis along, and y-axis perpendicular to the NW (see Figure 3). The 3D coherent intensity distribution around each diffraction peak was measured by recording the scattered X-rays from the specimen by the 2D detector at different incidence angles in a range of about $\pm 0.4^\circ$ around the Bragg angle with 160 angular steps and 5 s of exposure time.

3. Results

3.1. Free-Lying Nanowires

First, we have investigated a series of free-lying NWs without contacting electrodes. The 3D distribution of coherently scattered intensity in the vicinity of a $10\bar{1}0$ GaN Bragg peak of the free-lying NWs in the laboratory frame is shown in Figure 4. The intensity distribution of a free-lying NW of 350 nm in size is presented in Figure 4a,b and demonstrates

well pronounced hexagonal symmetry with the fringes originating from the opposite facets of the NW. There is only a single star-shaped Bragg peak distribution in reciprocal space (see Figure 4b), which indicates that this NW does not have a significant structural change and may be considered as a deformation-free NW. Several other investigated free-lying NWs of the same size demonstrated similar structure of the Bragg peak distribution in reciprocal space (see Supplementary Materials).

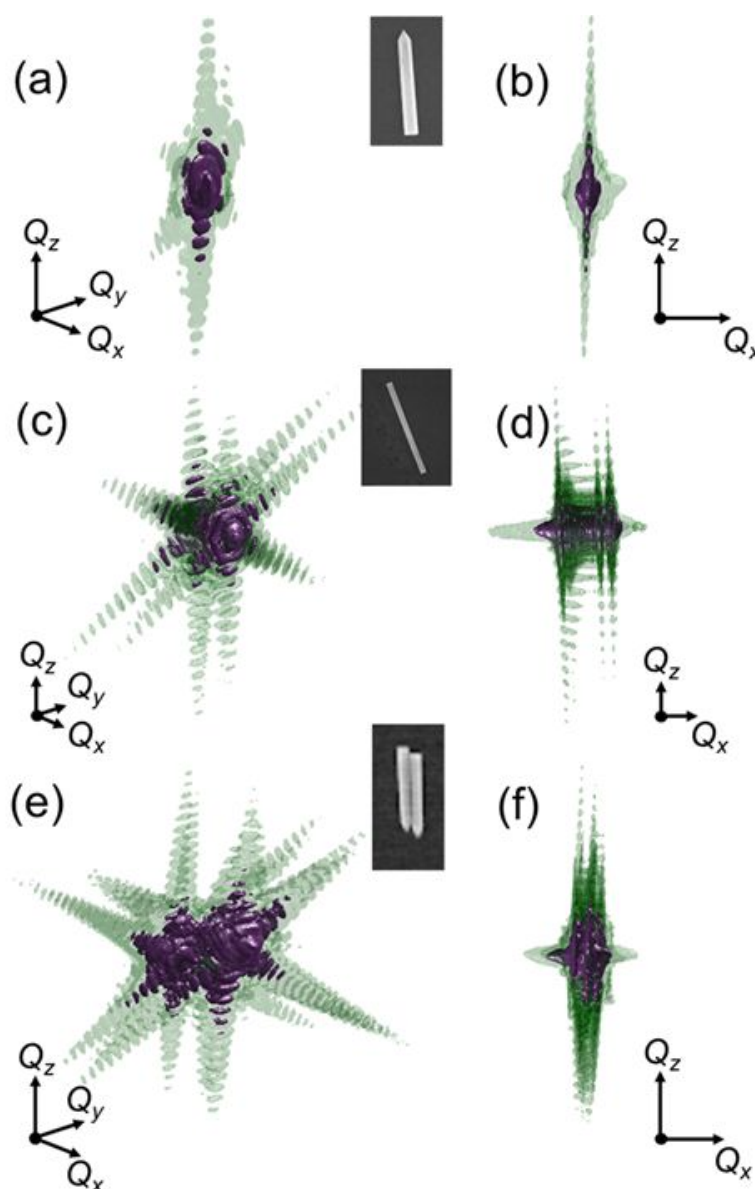


Figure 4. The intensity distribution around $10\bar{1}0$ GaN Bragg reflection of free-lying GaN NWs shown from two different views to emphasize the diffraction pattern details. (a–d) Single GaN NWs with the diameters of 350 nm (a,b) and 200 nm (c,d). The thinner 200 nm NW reveals a double Bragg peak structure due to its bending on the substrate (see text for details). (e,f) For a comparison, the intensity distribution of two NWs with the diameters of 350 nm lying close to each other form well separated Bragg peaks in reciprocal space. To enhance the diffraction pattern details, the intensity distributions are represented by two different iso-surfaces. The length of coordinate arrows corresponds to 0.1 nm^{-1} . The intensity is normalized to the maximum and the iso-surface values are 10^{-3} and $10^{-4.5}$ (a,b), $10^{-0.5}$ and 10^{-1} (c,d), $10^{-0.5}$ and 10^{-1} (e,f).

Further, a single, free-lying GaN NW with a smaller diameter of 200 nm was studied. Its intensity distribution is shown from two different directions in Figure 4c,d. Interestingly,

the diffraction pattern reveals the “double-star” structure of the Bragg peak distribution (see Figure 4d). Two additionally studied 200 nm free-lying GaN NWs demonstrated similar double structure of the Bragg peak intensity distribution (see Supplementary Materials), which is due to the bending of the NWs [22].

For comparison, a diffraction pattern of $10\bar{1}0$ GaN Bragg peak of two close lying NWs with diameters of 350 nm is presented in Figure 4e,f. In this case of 350 nm thick NWs, two well-separated hexagonal-star Bragg peaks are distinguishable in reciprocal space.

Therefore, it is possible to conclude that the free-lying GaN NWs with the diameter of 200 nm are already bent in contrast to 350 nm in diameter NWs. This effect makes investigation of the NWs with the diameters smaller than 350 nm more complicated.

3.2. Influence of Contacts on the NWs Structure

The 3D intensity distribution around $10\bar{1}0$ GaN Bragg peak for the contacted nanowires is shown in Figure 5. It is well seen in Figure 5a that the Bragg peak of the contacted 350 nm thick GaN NW has obtained an additional Bragg peak due to the induced strain from the deposited contacts.

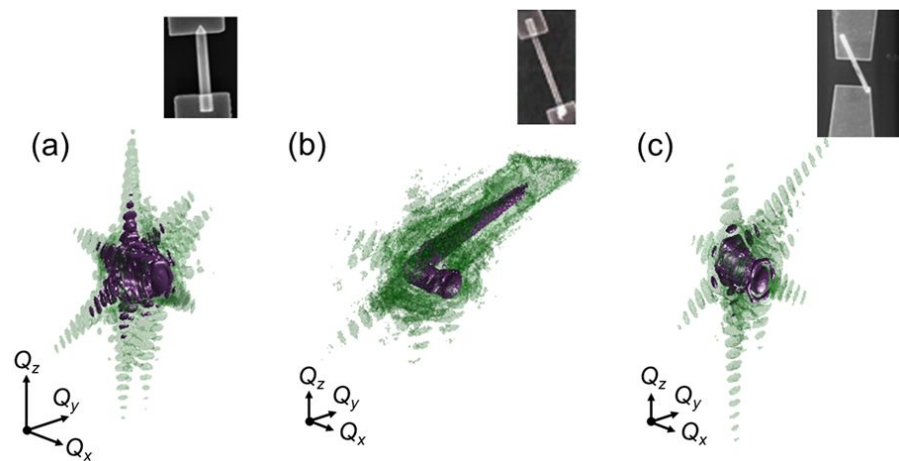


Figure 5. Comparison of the intensity distributions around $10\bar{1}0$ GaN NWs Bragg peak for the different types of Au contacts. (a,b) The contacts deposited on the top of the nanowires with the diameters of 350 nm (a) and 200 nm (b). (c) The intensity distribution for a NW with the diameter of 200 nm contacted on the top of the Au electrodes by melting procedure. For all types of the contacts, a significant influence on the scattered X-ray intensity due to the induced strain during the contacting process could be seen. To enhance the diffraction pattern details, the intensity distributions are represented by two different iso-surfaces. The length of coordinate arrows corresponds to 0.1 nm^{-1} . The intensity is normalized to the maximum and the iso-surface values are $10^{-3.5}$ and $10^{-4.5}$ (a), $10^{-1.5}$ and $10^{-2.85}$ (b), $10^{-2.5}$ and $10^{-3.5}$ (c).

The free-lying 200 nm thin GaN NWs were already bent before contacts deposition, but the bending angle was increased by 2 degrees after the contacts were applied (see Figure 5b). The nanowire fixation and bending mechanism were different for 350 nm and the 200 nm GaN NWs as can be seen from comparison of corresponding diffraction patterns (see Figure 5a,b).

Further, influence of the second type of Au contacts on the GaN NWs was studied (see Figure 2c). The corresponding distribution of intensity in reciprocal space around $10\bar{1}0$ GaN Bragg peak of a contacted 200 nm GaN NW is presented in Figure 5c, and shows the bending effect. Finally, we can conclude that all investigated types of contacts had a similar bending effect on the GaN NWs.

3.3. Operando Studies of GaN NWs

To study properties of the GaN NWs with the diameter of 350 nm, we have applied voltage bias to their ends and followed the evolution of the $10\bar{1}0$ GaN Bragg diffraction pattern. The Bragg peak intensity distribution as a function of applied voltage is shown in Figure 6. It is clearly visible in the figure that the distance between the Bragg peaks increases with the voltage causing an additional redistribution of the coherently scattered radiation around the Bragg peaks. As was already discussed above, this deformation of the Bragg peak is attributed to the GaN NW bending due to its expansion caused by the piezo effect under the applied voltage. The scheme of the bent NW and its intensity distribution in reciprocal space is shown in Figure 7a. The gap between two peaks increased with the applied voltage till the maximum elongation at two volts (see Figure 6d). After this critical value, the applied voltage bias was increased to five volts, and the NW was destroyed. Therefore, we assumed that the breakdown voltage of the system “GaN NW + Au contacts” was between two and five volts. The SEM images of the NWs after the breakdown voltage was applied are presented in the Supplementary Materials.

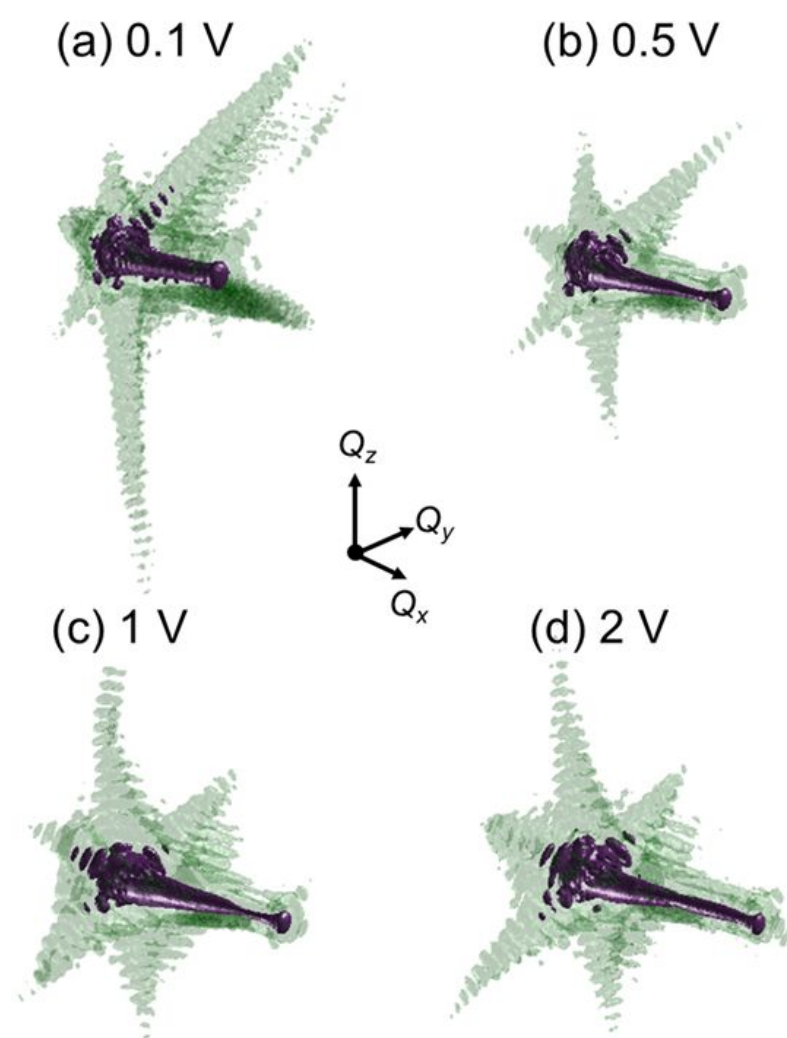


Figure 6. Evolution of intensity distribution around $10\bar{1}0$ GaN Bragg reflection of a contacted GaN NW with the diameter of 350 nm. The values of the applied voltage bias: 0.1 V (a), 0.5 V (b), 1 V (c), 2 V (d). To enhance the diffraction pattern details, the intensity distributions are represented by two different iso-surfaces. The length of coordinate arrows corresponds to 0.1 nm^{-1} . The intensity is normalized to the maximum and the iso-surface values are $10^{-3.4}$ and 10^{-4} .

Investigation of the applied voltage to the GaN NWs with a diameter of 200 nm was not successful due to the unstable contacts between the NWs and the metallic contacts. The 200 nm GaN NW positioned on the top of the second type of Au contacts was lost after the first applied voltage bias of 0.5 volts. In this situation, one can only conclude that this type of NW fixation is much weaker than the variant with the Au contacts on the top of the NW.

4. Discussion

To analyze the bending effect of the GaN NWs, a model of such bending was developed based on our previous results (see Ref. [22]). A scheme of the intensity distribution in reciprocal space is shown in Figure 7a. It explains relation between the bending angle $\theta = \arctan(q/|H_{10\bar{1}0}|)$ of the NW and the elongation q of the gap between two star-like Bragg peaks with the known length of the scattering vector $H_{10\bar{1}0}$.

To relate this bending angle with the split of the Bragg peak observed in the experiment and caused by this bending, we performed finite element method (FEM) simulations [25]. The lattice constants were considered to be $a_{\text{GaN}} = 3.189 \text{ \AA}$, $c_{\text{GaN}} = 5.178 \text{ \AA}$ for the wurzite GaN crystal [26]. Since the GaN has a transversely isotropic structure of the unit cell, the full stiffness matrix is given by five independent components. The elasticity constants C_{ij} of the GaN used in the model were the following: $C_{11} = 374 \text{ GPa}$, $C_{12} = 138 \text{ GPa}$, $C_{13} = 101 \text{ GPa}$, $C_{33} = 395 \text{ GPa}$, $C_{44} = 98 \text{ GPa}$ [27]. The equilibrium shape of the NW used in FEM simulations is shown in Figure 7b. The incident Gaussian beam profile with one micrometer full width at half maximum (FWHM) and 3D displacement field from the FEM model were used to simulate the intensity distribution in reciprocal space, which was compared with the experimental one. Varying displacement field in the model, the best correspondence between the angular distance of the Bragg peaks in the model simulations and experimental data were determined.

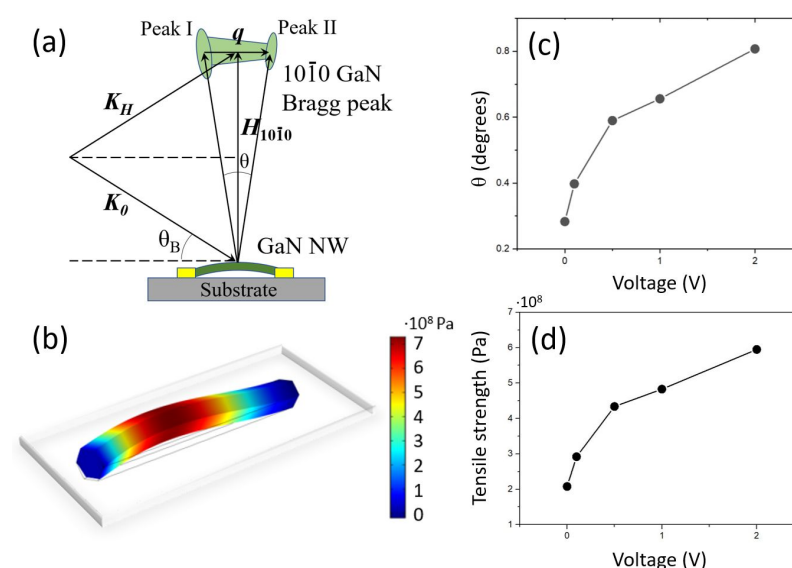


Figure 7. (a) Scheme of reciprocal space X-ray intensity distribution formation. (b) 3D FEM model of the bent GaN NW. The color scale bar gives values of the tensile strength obtained in this model. (c) Bending angle θ of the NW with the size of 350 nm as a function of the applied voltage bias. (d) Maximum tensile strength in the NW under voltage bias. The stress in the NW is increased from 2×10^8 Pa up to the ultimate tensile strength of 6×10^8 Pa, at which the NW was broken.

For the free-lying NW with the diameter of 200 nm, an average bending angle of 0.45 degrees was calculated from the distance q between two peaks in reciprocal space (see Figure 4c,d) that, according to FEM modelling, corresponds to the maximum tensile strength in the NW of about 3.4×10^8 Pa.

The bending angle of the contacted 350 nm GaN NWs was found to be 0.28 degrees and corresponds to 2×10^8 Pa tensile strength obtained from the FEM model. In our

previous experiment, the GaN NW was bent to 0.4 degrees after the Au contacts deposition with the tensile strength of 3×10^8 Pa, which supports the current findings. For the second type of Au contacts shown in Figure 5c we determined the angle of 0.29 degrees that corresponds to the tensile strength of 2.1×10^8 Pa.

Dependence of the bending angle θ between the two peaks of the $10\bar{1}0$ GaN Bragg reflection for the GaN NW under operando conditions is given in Figure 7c as a function of the voltage bias. From the FEM simulations, the maximum tensile strength value of the most top part of the nanowire was obtained for different bending angles measured in the experiment. Dependence of this tensile strength as a function of applied voltage bias is presented in Figure 7d. The strain in the GaN NW increased from 2×10^8 Pa up to 6×10^8 Pa, at which the nanostructure was broken. In general, the strain values are in a good agreement with the dependence observed in our previous study, but the voltage values corresponding to the same bending angles are five times smaller. We attribute this discrepancy to the different geometric parameters of the contacts, which were thicker this time and had different overlap with the NWs. The ultimate tensile strength at the breakdown voltage could be estimated with rather large error from the extrapolation of the obtained tensile strength dependence, but will be in a range of the previously obtained value of about 1 GPa.

5. Summary and Outlook

In our study, a strong influence of the different types of metallic contacts on the strain state of GaN NWs with diameters of 200 nm and 350 nm was demonstrated using coherent X-ray diffraction of the $10\bar{1}0$ GaN Bragg peak. Employing the developed FEM model, the maximum tensile strength in the nanowires was calculated for the different bending states induced due to the deposited Au contacts.

For the NWs with 350 nm in diameter, the maximum tensile strength raised to 2×10^8 Pa after the contacts deposition. Further, the influence of the applied voltage bias on the strain field evolution until the breakdown of the nanostructures was investigated. The strain in the GaN NWs increased up to the ultimate tensile strength of 6×10^8 Pa corresponding to two volts of applied bias, at which the nanowire was broken. This ultimate tensile strength was in a good agreement with our previous work, while the breakdown voltage deviation was explained by the different geometry of the contacts and their possibly different breakdown behavior.

In the case of the NWs with the diameter of 200 nm, it was demonstrated that they bend already by the interaction with the substrate. The applied Au contacts disturbed the scattered X-ray intensity distribution of the Bragg peak even more. Additionally, the contacts fixation of this type of NWs was less stable, which made their investigation with the current diameter to length ratio rather challenging. For our future experiments, the length of the NWs with diameters below 350 nm is planned to be shorter than 2 μ m.

An additional type of fixation with the NWs positioned on the top of the Au contacts demonstrated for the GaN NWs with the diameter of 200 nm a much weaker “contact-nanostructure” fixation. The GaN NW was disconnected already after the first applied voltage bias of 0.5 volts. Due to these reasons, the operando study of the nanowires with this type contacts was not successful.

We expect that the results of our work will contribute to the development and manufacture of the devices based on the nanostructures and may help the high-technology industry development.

Supplementary Materials: The following are available online at <https://www.mdpi.com/article/10.3390/app11209419/s1>, Section S1: Free-lying NWs; Section S2: SEM images of the contacted NWs before and after the experiment; Section S3: Evolution of the scattered intensity of the NWs as a function of applied voltage; Section S4: Measurements of the GaN NWs with the Pt contacts. Figure S1: (a–c) The intensity distribution around $10\bar{1}0$ GaN Bragg reflection of three different free-lying GaN NWs with diameters of 350 nm. (d–f) The same Bragg peaks from a different view perpendicular to the [0001] crystallographic direction. The figures demonstrate absence of the “double-star” structure,

which was observed in the case of bent GaN NWs. Figure S2: (a,b) The intensity distribution around $10\bar{1}0$ GaN Bragg peak of two free-lying GaN NWs with diameters of 200 nm. (c,d) A different view of these Bragg peaks from a direction perpendicular to the $[0001]$ crystallographic axis. The Bragg peaks demonstrate the “double-star” structure typical for the bent GaN NWs. Figure S3: SEM images of the contacted GaN NWs. The first 350 nm GaN NW before (a) and after (b) applied voltage bias. The second 350 nm GaN NW before (c) and after (b) the maximum applied voltage. The 200 nm GaN NW before (e) and after (f) the applied voltage bias. Figure S4: SEM images of the second type of Au contacts. The NW with the diameter of 200 nm contacted on the top of the Au electrodes by melting procedure before (a) and after (b) applied 0.1 V of bias. (c) The 350 nm GaN NW on the top of Au contacts. Figure S5: Evolution of the intensity distribution around $10\bar{1}0$ GaN Bragg reflection of the second contacted GaN NW with the diameter of 350 nm. The values of the applied voltage bias: 0 V (a), 1 V (b), 2 V (c), 5 V (d). Figure S6: Dependence of the scattering vector modulus ($H_{10\bar{1}0}$) on the applied voltage bias for the first (a) and second (b) 350 nm GaN NW. Similar dependence of the scattering vector modulus ($H_{10\bar{1}0}$) on the applied voltage bias for the first (c) and second (d) 200 nm GaN NW. Figure S7: Dependence of the bending angle for the first (a) and second (b) GaN NW with the diameter of 200 nm on the applied voltage bias. Figure S8: SEM images of the Pt contacted 200 nm GaN NWs. Figure S9: (a) SEM images of the Pt contacted GaN NW with diameter of 200 nm. (b) Comparison of the diffracted intensity of the $10\bar{1}0$ GaN Bragg reflection of the NW before (up) and after (bottom) deposition of the Pt contacts. (c) 3D intensity distribution around $10\bar{1}0$ GaN Bragg reflection of the NW.

Author Contributions: Conceptualization and methodology, S.L. and I.A.V.; sample preparation, Z.B., A.N., A.M., and L.S.; sample characterization, A.J. and T.F.K.; X-ray experiment, S.L., Y.Y.K., L.G., I.A.Z., R.K., D.D., M.S., and I.A.V.; data analysis, S.L., Y.Y.K., and D.D.; writing—review and editing, S.L. and I.A.V. All authors have read and agreed to the published version of the manuscript.

Funding: This research was funded by the Helmholtz Associations Initiative Networking Fund (Grant No. HRSF-0002) and the Russian Science Foundation (Grant No. 18-41-06001); Sergey Lazarev was funded by the Competitiveness Enhancement Program Grant of Tomsk Polytechnic University and the Governmental program “Science,” project no. FSWW-2020-0014.

Data Availability Statement: The data presented in this study are openly available in Zenodo.org at <https://zenodo.org/record/5520539#.YUshJ44zaF4> at doi:10.5281/zenodo.5520539, reference number [28].

Acknowledgments: We acknowledge DESY (Hamburg, Germany), a member of the Helmholtz Association HGF, for the provision of experimental facilities. Parts of this research were carried out at PETRA III and DESY NanoLab and we would like to thank the beamline staff for assistance in using coherence applications beamline P10. The authors are thankful to E. Weckert for the support of the project and also acknowledge a careful reading of the manuscript by Z. Ren.

Conflicts of Interest: The authors declare no conflicts of interest.

References

1. Kuykendall, T.; Ulrich, P.; Aloni, S.; Yang, P. Complete composition tunability of InGaN nanowires using a combinatorial approach. *Nat. Mater.* **2007**, *6*, 951–956. [\[CrossRef\]](#)
2. Huang, C.T.; Song, J.; Tsai, C.M.; Lee, W.F.; Lien, D.H.; Gao, Z.; Hao, Y.; Chen, L.J.; Wang, Z.L. Single-InN-Nanowire Nanogenerator with Upto 1 V Output Voltage. *Adv. Mater.* **2010**, *22*, 4008–4013. [\[CrossRef\]](#) [\[PubMed\]](#)
3. *Semiconductor Nanowires: From Next-Generation Electronics to Sustainable Energy*; Lu, W., Xiang, J., Eds.; The Royal Society of Chemistry: London, UK, 2015.
4. Dasgupta, N.P.; Sun, J.; Liu, C.; Brittman, S.; Andrews, S.C.; Lim, J.; Gao, H.; Yan, R.; Yang, P. 25th Anniversary article: semiconductor nanowires—Synthesis, characterization, and applications. *Adv. Mater.* **2014**, *26*, 2137–2184. [\[CrossRef\]](#)
5. Monemar, B.; Ohlsson, B.J.; Gardner, N.F.; Samuelson, L. Nanowire-Based Visible Light Emitters, Present Status and Outlook. In *Semiconductors and Semimetals*; Dayeh, S.A., Fontcuberta i Morral, A., Jagadish, C.H., Eds.; Elsevier: Amsterdam, The Netherlands, 2016; Volume 94, pp. 227–271.
6. Li, C.; Wright, J.B.; Liu, S.; Lu, P.; Figiel, J.J.; Leung, B.; Chow, W.W.; Brener, I.; Koleske, D.D.; Luk, T.S.; Feezell, D.F.; Brueck, S.R.J.; Wang, G.T. Nonpolar InGaN/GaN Core-Shell Single Nanowire Lasers. *Nano Lett.* **2017**, *17*, 1049–1055. [\[CrossRef\]](#) [\[PubMed\]](#)
7. *III-Nitride Materials, Devices and Nano-Structures*; Feng, Z.C., Ed.; World Scientific Publishing Company Pte Limited: Singapore, 2017.

8. Borgström, M.T.; Magnusson, M.H.; Dimroth, F.; Siefert, G.; Höhn, O.; Riel, H.; Schmid, H.; Wirths, S.; Björk, M.; Åberg, I.; et al. Towards Nanowire Tandem Junction Solar Cells on Silicon. *IEEE J. Photovolt.* **2018**, *8*, 733–740. [\[CrossRef\]](#)
9. Bi, Z.; Chen, Z.; Danesh, F.; Samuelson, L. From nanoLEDs to the realization of RGB-emitting microLEDs. In *Semiconductors and Semimetals*; Jiang, H., Lin, J., Eds.; Elsevier: Amsterdam, The Netherlands, 2021; Volume 106, pp. 223–251.
10. Newton, M.C.; Leake, S.J.; Harder, R.; Robinson, I.K. Three-dimensional imaging of strain in a single ZnO nanorod. *Nat. Mater.* **2010**, *9*, 120–124. [\[CrossRef\]](#) [\[PubMed\]](#)
11. Godard, P.; Carbone, G.; Allain, M.; Mastropietro, F.; Chen, G.; Capello, L.; Diaz, A.; Metzger, T.H.; Stangl, J.; Chamard, V. Three-dimensional high-resolution quantitative microscopy of extended crystals. *Nat. Commun.* **2011**, *2*, 568. [\[CrossRef\]](#)
12. Hruszkewycz, S.O.; Holt, M.V.; Murray, C.E.; Bruley, J.; Holt, J.; Tripathi, A.; Shpyrko, O.G.; McNulty, I.; Highland, M.J.; Fuoss, P.H. Quantitative nanoscale imaging of lattice distortions in epitaxial semiconductor heterostructures using nanofocused X-ray Bragg projection ptychography. *Nano Lett.* **2012**, *12*, 5148–5154. [\[CrossRef\]](#) [\[PubMed\]](#)
13. Dzhigaev, D.; Shabalin, A.; Stankevič, T.; Lorenz, U.; Kurta, R.P.; Seiboth, F.; Wallentin, J.; Singer, A.; Lazarev, S.; Yefanov, O.M.; et al. Bragg coherent x-ray diffractive imaging of a single indium phosphide nanowire. *J. Opt.* **2016**, *18*, 064007. [\[CrossRef\]](#)
14. Dzhigaev, D.; Stankevič, T.; Bi, Z.; Lazarev, S.; Rose, M.; Shabalin, A.; Reinhardt, J.; Mikkelsen, A.; Samuelson, L.; Falkenberg, G.; et al. X-ray Bragg Ptychography on a Single InGaN/GaN Core-Shell Nanowire. *ACS Nano* **2017**, *11*, 6605–6611. [\[CrossRef\]](#)
15. Vartanyants, I.A.; Yefanov, O.M. *X-ray Diffraction. Modern Experimental Techniques. Coherent X-Ray Diffraction Imaging of Nanostructures*; Pan Stanford Publishing: Singapore, 2015; Chapter 12, pp. 341–384.
16. Fienup, J.R. Phase retrieval algorithms: a comparison. *Appl. Opt.* **1982**, *21*, 2758–2769. [\[CrossRef\]](#) [\[PubMed\]](#)
17. Marchesini, S. Invited article: A unified evaluation of iterative projection algorithms for phase retrieval. *Rev. Sci. Instrum.* **2007**, *78*, 011301. [\[CrossRef\]](#) [\[PubMed\]](#)
18. Vartanyants, I.A.; Robinson, I.K. Partial coherence effects on the imaging of small crystals using coherent x-ray diffraction. *J. Phys. Condens. Mat.* **2001**, *13*, 10593. [\[CrossRef\]](#)
19. Abuin, M.; Kim, Y.Y.; Runge, H.; Kulkarni, S.; Maier, S.; Dzhigaev, D.; Lazarev, S.; Gelisio, L.; Seitz, C.; Richard, M.I.; et al. Coherent X-ray Imaging of CO-Adsorption-Induced Structural Changes in Pt Nanoparticles: Implications for Catalysis. *ACS Appl. Nano Mater.* **2019**, *2*, 4818–4824. [\[CrossRef\]](#)
20. Kawaguchi, T.; Keller, T.F.; Runge, H.; Gelisio, L.; Seitz, C.; Kim, Y.Y.; Maxey, E.R.; Cha, W.; Ulvestad, A.; Hruszkewycz, S.O.; et al. Gas-Induced Segregation in Pt-Rh Alloy Nanoparticles Observed by In Situ Bragg Coherent Diffraction Imaging. *Phys. Rev. Lett.* **2019**, *123*, 246001. [\[CrossRef\]](#)
21. Kim, Y.Y.; Keller, T.F.; Goncalves, T.J.; Abuin, M.; Runge, H.; Gelisio, L.; Carnis, J.; Vonk, V.; Plessow, P.N.; Vartanyants, I.A.; et al. Single Alloy Nanoparticle X-Ray Imaging during a Catalytic Reaction. *arXiv* **2021**, arXiv:2103.01573.
22. Lazarev, S.; Dzhigaev, D.; Bi, Z.; Nowzari, A.; Kim, Y.Y.; Rose, M.; Zaluzhnyy, I.A.; Gorobtsov, O.Y.; Zozulya, A.V.; Lenrick, F.; et al. Structural Changes in a Single GaN Nanowire under Applied Voltage Bias. *Nano Lett.* **2018**, *18*, 5446–5452. [\[CrossRef\]](#) [\[PubMed\]](#)
23. Hersee, S.D.; Sun, X.; Wang, X. The controlled growth of GaN nanowires. *Nano Lett.* **2006**, *6*, 1808–1811. [\[CrossRef\]](#) [\[PubMed\]](#)
24. Stierle, A.; Keller, T.F.; Noei, H.; Vonk, V.; Roehlsberger, R. DESY NanoLab. *J. Large Scale Res. Facil. JLSRF* **2016**, *2*, A76. [\[CrossRef\]](#)
25. Reddy, J.N. *An Introduction to the Finite Element Method*, 3rd ed.; McGraw-Hill Professional; McGraw-Hill: New York, NY, USA, 2005.
26. Levinshstein, M.E.; Rumyantsev, S.L.; Shur, M.S. *Properties of Advanced Semiconductor Materials: GaN, AlN, InN, BN, SiC, SiGe*; John Wiley and Sons: Hoboken, NJ, USA, 2001.
27. Morales, F.M.; González, D.; Lozano, J.G.; García, R.; Hauguth-Frank, S.; Lebedev, V.; Cimalla, V.; Ambacher, O. Determination of the composition of $In_xGa_{1-x}N$ from strain measurements. *Acta Mater.* **2009**, *57*, 5681–5692. [\[CrossRef\]](#)
28. Lazarev, S.; Kim, Y.Y.; Gelisio, L.; Zhaoxia, B.; Nowzari, A.; Zaluzhnyy, I.A.; Khubbutdinov, R.; Dzhigaev, D.; Jeromin, A.; Keller, T.F.; et al. Raw Data Repository for the Article: Influence of Contacts and Applied Voltage on a Structure of a Single GaN Nanowire. *arXiv* **2021**, arXiv:2108.10173. doi:10.5281/zenodo.5520539.